ChemCatChem

Research Article
doi.org/10.1002/cctc.202400988

Chemistry Europe
European Chemical Societies Publishing

www.chemcatchem.org

Operando Surface X-Ray Diffraction Studies of Epitaxial Co_3O_4 and CoOOH Thin Films During Oxygen Evolution: pH Dependence

Canrong Qiu,[a] Fouad Maroun,*[b] Mathilde Bouvier,[b] Ivan Pacheco,[b] Philippe Allongue,*[b] Tim Wiegmann,[a] Carl Hendric Scharf,[a] Victor de Manuel-Gonzalez,[a] Finn Reikowski,[a] Jochim Stettner,[a] and Olaf M. Magnussen*[a]

Transition metal oxides, especially cobalt oxides and hydroxides, are of great interest as precious metal free electrode materials for the oxygen evolution reaction (OER) in electrochemical and photoelectrochemical water splitting. Here, we present detailed studies of the potential- and pH-dependent structure and structural stability of Co_3O_4 and CoOOH in neutral to alkaline electrolytes (pH 7 to 13), using *operando* surface X-ray diffraction, atomic force microscopy, and electrochemical measurements. The experiments cover the pre-OER and OER range and were performed on epitaxial Co_3O_4(111) and CoOOH(001) films electrodeposited on Au(111) single crystal electrodes. The CoOOH films were structurally perfectly stable under all experimental conditions, whereas Co_3O_4 films exhibit at all pH values reversible potential-dependent structural transformations of a sub-nanometer thick skin layer region at the oxide surface, as reported previously for pH 13 (F. Reikowski et al., ACS Catal. 2019, 9, 3811). The intrinsic OER activity at 1.65 V versus the reversible hydrogen electrode decreases strongly with decreasing pH, indicating a reaction order of 0.2 with respect to $[OH^-]$. While the Co_3O_4 spinel is stable at pH 13, intermittent exposure to electrolytes with $pH \leq 10$ results in dissolution as well as gradual degradation of its OER activity in subsequent measurements at pH 13.

1. Introduction

The storage of natural intermittent energy, such as wind or solar power, necessitates sustainable energy conversion techniques that can produce commercially valuable chemicals. Photoelectrochemical and electrochemical water-splitting have been emerging as a promising technique for this purpose.[1,2] One key bottleneck in water-splitting is the oxygen evolution reaction (OER), which requires transfer of four protons and electrons and thus is kinetically sluggish. Transition-metal oxides, in particular cobalt (hydr)oxide materials, have been identified as promising OER catalysts, since they are earth-abundant, efficient, and scalable over a wide range of electrochemical conditions.[3–8] The stability of such materials can extend from alkaline to neutral electrolyte without a serious degradation of catalytic performance. Extensive research has been performed, aiming at developing different synthesis methods to produce Co-based catalyst materials as well as obtaining deeper insights into the nature of the OER process.[3,9–15]

Although tremendous efforts have been devoted to study the OER mechanism on Co-oxide catalysts, fundamental understandings that relate the OER reactivity to the atomic scale surface structure remains elusive. The challenges stem essentially from the difficulties of characterizing the reactive surface of the catalyst under reaction conditions. Previous studies have shown for some Co-oxide materials, such as Co_3O_4, a reversible and highly dynamical structural transition of the near-surface region under OER conditions, where a skin layer without long-range ordering is formed.[14–18] Furthermore, most studies up to now have been performed on polycrystalline materials, which exhibit multiple surface orientations, structural defects, and ill-defined electrochemical surface area (ECSA), making precise correlations between the measured OER current density and OER reaction sites difficult. Only in a few cases, studies of structurally well-defined OER catalyst materials with defined surface orientation have been performed.[16–22]

Apart from the catalyst material, also the electrolyte composition plays a major role in the OER reaction. Especially the pH has been recognized as a potential factor that may influence the OER mechanism by changing the protonation state of OER sites.[23] Depending on whether the transfer of proton and electrons occurs simultaneously or sequentially, a pH independent or pH dependent OER current density relative to the reversible hydrogen electrode (RHE) potential scale will

---

[a] C. Qiu,+ T. Wiegmann, C. Hendric Scharf, V. de Manuel-Gonzalez, F. Reikowski, J. Stettner, O. M. Magnussen
Institute of Experimental and Applied Physics, Kiel University, 24098 Kiel, Germany
E-mail: magnussen@physik.uni-kiel.de

[b] F. Maroun, M. Bouvier, I. Pacheco, P. Allongue
Physique de la Matière Condensée, Ecole Polytechnique, CNRS, Palaiseau, France
E-mail: fouad.maroun@polytechnique.edu
philippe.allongue@polytechnique.edu

Supporting information for this article is available on the WWW under https://doi.org/10.1002/cctc.202400988 be expected, respectively.[24] Apart from this, the solution pH also affects the stability of catalyst material. In acidic and neutral electrolytes, Co oxide materials tend to dissolve, inducing a detrimental effect to the overall OER performance.[20,25,26] These effects are relevant not only for a complete understanding of the OER mechanism but also their application as anode materials in electrocatalytic water splitting, as prolonged electrolysis was found to gradually decrease the pH near the anode-electrolyte interface. Furthermore, OER in weakly alkaline to neutral electrolyte is of interest for photoelectrochemical water splitting and as the counter reaction in electrochemical CO_2 reduction. Very recently, chemically modified Co oxide electrocatalysts were also found to be stable and reactive under highly acidic conditions, albeit these studies were not performed on structurally well-defined samples.[27–32]

In this work, we address the influence of pH (in the range 7 to 13) on the catalyst structure and OER activity by studies of well-defined epitaxial Co_3O_4(111) and CoOOH(001) developed in our recent work.[16,17,33] These previous *operando* surface X-ray diffraction measurements in 0.1 M NaOH revealed a pronouncedly different behavior of the two types of catalysts. The CoOOH samples were perfectly stable during potential cycles into the OER regime. In contrast, the Co_3O_4 films undergo the reversible formation of (sub−)nanometer thick skin layers with an amorphous structure, accompanied by a contraction of the Co_3O_4 bulk lattice. This transformation of the oxide surface started at a potential well before the OER onset, indicating that the skin layer forms because of the intrinsic Co redox electrochemistry rather than due to the OER process. In more recent work, we showed that the OER activity scales with the effective skin layer thickness, suggesting that the skin layer is a three-dimensional OER-active region.[17] We also demonstrated using operando SXRD/XAS that the Co oxidation state in the skin layer is 3+.[18] These studies were performed solely in alkaline solution at pH 13.

We here investigate the influence of solution pH on the electrochemical behavior and the potential-dependent structure of epitaxial Co oxide thin films in the pre-OER and OER regime. For this, a combination of *operando* SXRD, electrochemical and optical reflectivity measurements, and *ex situ* AFM was employed to study Co_3O_4(111) and CoOOH(001) films in the pH range from 7 to 13. As discussed in detail elsewhere,[17] the film morphology has a large influence on the electrochemical and structural properties of these oxide materials. We therefore performed the studies at different pH subsequently on the same samples, which enables a rigorous comparison.

Experimental Methods

Sample Preparation and Characterization

All cobalt oxide thin films were grown on Au(111) substrate using an electrodeposition technique adapted from the method of Koza et al.[12] CoOOH films were directly deposited on Au(111). The Co_3O_4 film was deposited on a (001)-oriented CoOOH film on Au(111), since this was found to result in a smoother surface than a single layer Co_3O_4 film on Au(111).[17,33] The films were deposited on hat-shaped Au(111) single crystals (MaTeck) with an active electrode surface of 4 mm diameter and a miscut $<0.1°$. All films were grown by the same general procedure, with the difference being only different concentrations of NaOH. Prior to film preparation, the Au substrates were soaked in a hot 1:2 mixture of 30% H_2O_2 and 96% H_2SO_4 (Carlo Erba, RSE) for 1 min to remove residual film materials from earlier experiments and then annealed in a butane flame for 5 min. Electrodeposition of CoOOH films was performed in an oxygen-free Co^{2+} solution, containing 1 mM $Co(NO_3)_2$, 1.2 mM sodium tartrate and 5 M NaOH, prepared by mixing degassed Mili-Q water with high purity chemicals of Co nitrate (Merck, 99%), Na tartrate (Sigma-Aldrich, ACS reagent, 99.5%), and NaOH (Merck, ACS reagent, Fe content <0.0005%). The Co^{2+} solution was electrooxidized at −0.55 V vs. a mercury sulfate reference electrode in a customized home-built electrodeposition cell at a reflux temperature of ≈103 °C. A charge of 8 mC/cm^2 was passed, resulting in the deposition of a film with an average thickness of 15–25 nm. After the deposition, the sample was rinsed with ultrapure water and dried under a gentle nitrogen gas stream (purity >99.999%). To further obtain the $Co_3O_4|CoOOH$ bilayer films (in the following denoted as Co_3O_4 for simplicity), the electrodeposition procedure was repeated in an electrolyte solution containing 1 M instead of 5 M NaOH.

The sample morphology was characterized under ambient conditions using either a Agilent PicoPlus or a Bruker Dimension V atomic force microscope (AFM) in tapping mode. In AFM measurements of electrochemically treated samples, the sample was quickly rinsed after emersion from the cell with ultrapure water to remove residual electrolyte at surface and then dried under a jet of N_2 gas (99.999% purity) for 1 minute.

Surface X-Ray Diffraction, Electrochemical, and Optical Reflectivity Measurements

For the SXRD and electrochemical studies the sample was transferred to a custom-build cell that allows simultaneous electrochemical and *operando* X-ray diffraction measurement. The hat-shaped crystal was sealed in the cell with a Teflon gasket, leaving only the Co oxide coated Au(111) surface exposed to the electrolyte. The cell volume above the electrolyte solution was continually purged with Ar gas (6.0) to maintain an oxygen-free atmosphere. The solution exchange was achieved using a computer-controlled syringe pump system. With this pump system, the electrolyte was continually flown through the sample at an adjustable rate of 5–10 ul/s to remove radiolysis products that potentially might be generated by the X-ray beam as well as oxygen gas produced in the OER. This electrolyte flow also facilitated mass transport in the electrolyte, which is of importance at the lower pH values. The electrochemical potential control was achieved using a potentiostat (Ivium) that connected the Au sample (working electrode) to a Ag/AgCl (3.4 M KCl) reference electrode (eDAQ) and a Pt wire counter electrode. To avoid Pt contamination, the Pt wire was placed in the outlet of the cell, i.e., downstream of the sample. All presented data are iR-corrected and are given with respective to the reversible hydrogen electrode to ease comparison of the electrochemistry data obtained at different pH.

The *operando* surface X-ray diffraction (SXRD) measurements were performed at the P23 beamline of PETRA III at DESY. The X-ray beam with a photon energy of 22.5 keV and a flux around 10^{12} photons/second was focused to 200 μm (width)×75 μm (height). A 2D LAMBDA 750 k GaAs detector (1556×516 pixels with each pixel being 0.05 μm×0.05 μm) was used to monitor the X-ray diffraction signal. The sample cell was mounted on a heavy load six-circle diffractometer (Huber). The incident angle was fixed at 2° in a vertical geometry mode during surface X-ray diffraction measurements. Under these conditions, the X-ray penetration depth in Co_3O_4 is 4 μm, i.e., the X-rays probe the entire oxide film. For describing the reciprocal space geometry, a hexagonal unit cell with unit cell vectors **a** = b = 2.884 Å and **c** = 7.064 Å was used, which corresponds to reciprocal space vectors of **a*** = b* = 2.51 $Å^{-1}$ and **c*** = 0.89 $Å^{-1}$. Here, the $\boldsymbol{q_z}$ direction (L axis) is oriented along surface normal, q_x and q_y (H and K axis) are located within the (111) surface plane (Figure 1a). To ease comparison with the literature, the Bragg peaks of the studied Co_3O_4 and CoOOH films were indexed according to the conventional cubic and hexagonal unit cells of these materials.

After sample alignment and initial characterization, *operando* SXRD measurements were performed by continually monitoring specific Bragg peaks of the Co oxide film with the 2D X-ray detector during potential cycles (employing typically 2–3 cycles in each separate measurement). For Co_3O_4 the $(1\bar{1}3)$ or (404) Bragg peak and for CoOOH the (017) Bragg peak was used. The detector images were recorded at a rate of 1 s^{-1}, allowing to study the structural dynamics at high time resolution. Parallel to the SXRD data, the electrochemical current and the optical reflectivity, obtained with a 630 nm laser diode at normal incidence, were measured. The upper potential limit of the potential cycles was set in each electrolyte at a value where the OER current density is $\leq$6.5 mA/cm^{-2}, while the lower limit of the potential window was chosen at about 1.0 V_{RHE}, which is slightly lower than the Co_3O_4/CoOOH redox potential (around 1.1 V_{RHE}).

To attain the Co oxide crystallite size as well as the lattice strain from the SXRD data, the intensity distribution at the diffraction peak in each 2D detector frame was first mapped to the reciprocal space using the diffraction geometry. Then, the peak center and width in the horizontal and vertical direction were determined by calculating one-dimensional projections of the peak intensity along horizontal and vertical direction and fitting these profiles by a pseudo-Voigt function. The peak positions $q_{\perp,\parallel}$ and full width at half maximum ($\mathrm{fwhm}_{\perp,\parallel}$) values, obtained from these fits, were used to calculate the film strain $\varepsilon_{\perp,\parallel} = \frac{q_{\perp,\parallel,\mathrm{nom}}}{q_{\perp,\parallel}} - 1$, where $q_{\perp,\parallel,\mathrm{nom}}$ are the peak positions that correspond to the literature values of the lattice parameters, and the coherence length $d_{\perp,\parallel} = 2\pi/\mathrm{fwhm}_{\perp,\parallel}$, which is associated with the grain size.

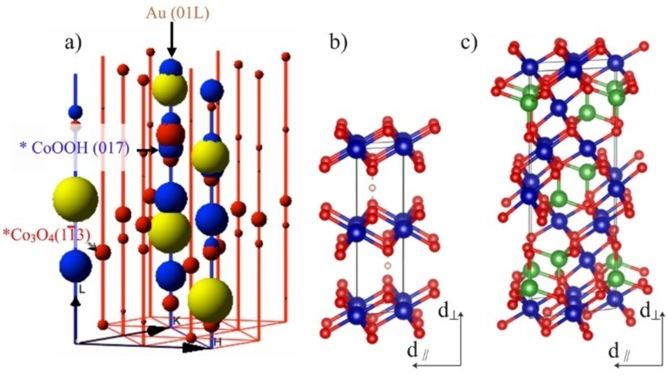

Figure 1. a) Reciprocal space geometry of Bragg peaks (spheres) and crystal truncation rods for Au(111) (yellow), the epitaxial Co_3O_4(111) film (red), and the epitaxial CoOOH(001) film (blue). The relative scattering intensities of the Bragg peaks are illustrated by the diameters of the spheres. In the employed hexagonal coordinate system the L axis is parallel to the Au[111] lattice vector, while the H and K axes are within the Au(111) plane. Within the surface plane, the $Co_3O_4[\bar{2}\bar{2}4]$ and the CoOOH[100] lattice vector are aligned with the H axis. Two Bragg peaks used for the *operando* studies, $Co_3O_4(1\bar{1}3)$ and CoOOH (017), are highlighted. (b,c) Crystal structures of (b) CoOOH and (c) Co_3O_4, with Co^{3+} atoms shown in blue, Co^{2+} atom in green, O atoms in red, and H atoms in white. In the chosen unit cells, the c axes are oriented along the surface normal for CoOOH(001) and Co_3O_4(111) epitaxial films (adapted from Ref.[16] Copyright American Chemical Society 2019).

Four electrolytes were used for the electrochemistry experiments: 0.1 M NaOH solution (pH 13), 0.1 M carbonate buffer solution of pH 10 (0.046 M $NaHCO_3$/0.054 M Na_2CO_3), 0.06 M phosphate buffer of pH 8 (0.056 M K_2HPO_4/0.004 M KH_2PO_4), and 0.06 M phosphate buffer of pH 7 (0.033 M K_2HPO_4/0.028 M KH_2PO_4). The same sample was sequentially measured in electrolytes of different pH, by exchanging the solutions with the pump system. In the experiments described in detail in the paper, the employed sequence of electrolytes was pH 13 (×1), pH 10 (×3), pH 13 (×1), pH 8 (×3), pH 13 (×1), pH 7 (×1), and pH 13 (×1) (in brackets the numbers of independent measurements in each electrolyte are given). To change the electrolyte to a different pH, the old electrolyte was drained completely from the cell under open circuit potential. Afterwards, the cell was quickly refilled with the next electrolyte and emptied again for 7 to 10 times. Then the cell was filled one last time and a resting potential of 1.37 V was applied before further measurements. This procedure took typically 10 minutes. The application of three sequential CVs at pH 10 and pH 8 served to monitor possible irreversible structural changes at lower pH.

2. Results

2.1. Structure and Morphology of as Prepared Co oxide Films

Figure 1a shows the position of Bragg peaks in reciprocal space, calculated for bulk oxyhydroxide CoOOH(001) (blue spheres) and bulk spinel oxide Co_3O_4(111) (red spheres) films in epitaxy with the Au(111) (yellow spheres) substrate, with the $Co_3O_4[\bar{2}\bar{2}4]$ and the CoOOH[100] lattice vector being oriented along the $Au[1\bar{1}0]$ direction.[16] The corresponding atomic models are presented in Figure 1b,c. Figure 2 shows the intensity distribution along the (01 L) rod of Au(111) measured for the Co_3O_4 sample deposited on a CoOOH(001) buffer layer (see scheme of the structure in inset). Besides the two intense Au(111) Bragg

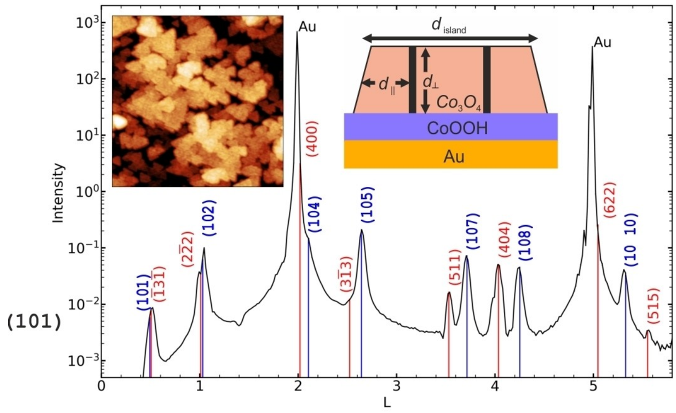

Figure 2. Structure and morphology of the Co_3O_4 model electrocatalysts. X-ray scattering intensity profile along the (01 L) crystal truncation rod of Au (111). Two sharp Bragg peaks (L = 2, 5) of the Au substrate are coexistent with weaker Bragg peaks, which are assigned to the epitaxial Co_3O_4 (red) and underlying CoOOH (blue) deposits. The Miller indices given for each Bragg peak refer to the conventional unit cells of Co_3O_4 (fcc) and CoOOH (hcp). In addition, a characteristic AFM image (1×1 μm^2) of the as-prepared film surface and a model illustrating the structural parameters are included as insets.

peaks (L = 2 and 5), all other peaks can be assigned to either (111)-oriented Co_3O_4 (red labels) or (001)-oriented CoOOH (blue labels), in agreement with the positions shown in Figure 1a. No other peaks are found. This is indicating that an epitaxial CoOOH(001) layer was deposited on Au(111) and that the Co_3O_4(111) layer grows epitaxially on the CoOOH(001) layer, in agreement with our previous work.[17,33]

For Co_3O_4, the vertical lattice spacing *c* is identical to the bulk value and in plane strains are negligible. For CoOOH a slight expansion of the *c* axis ($\leq 2\%$) is observed with substantial in plane tensile strains. The average crystallite dimensions are $d_\perp = 14.0$ nm and $d_{||} = 18.2$ nm for Co_3O_4 and $d_\perp = 11.7$ nm and $d_{||} = 23.5$ nm for CoOOH. In agreement with Ref.,[17] AFM images of the Co_3O_4 sample (see inset of Figure 2) reveal a granular morphology, consisting of tightly packed triangular islands with a flat top. The island edges are preferentially oriented along the 6 main in-plane directions and at 60° to each other. Their lateral size of $d_{island} \approx 100$ nm is larger than $d_{||}$, which indicates that the islands are composed of several crystallites. Nevertheless, no indication for grain boundaries could be resolved by AFM on top of the islands, suggesting that emerging grain boundaries are very narrow (see inset scheme in Figure 2).[17]

2.2. Electrochemical Characterizations

Figure 3a–g show CVs of a Co_3O_4 sample, recorded subsequently in electrolytes of different pH (in order a to g). Corresponding CVs of the CoOOH sample are presented in Figure 3h–i (recorded in order h–i). The current density is normalized to the geometric surface area of the electrode. The shapes of these CVs are in good agreement with the literature.[14–18] Both types of samples exhibit a large pseudocapacitive current over the entire studied potential range. In the case of CoOOH(001) (Figure 3h–i), the CVs are rather featureless in the pre-OER regime. In contrast, the CVs of the Co_3O_4(111) film (Figure 3a–g) exhibit two pairs of redox waves (A1/C1) located at around 1.1 V_{RHE} and at about 1.5 V_{RHE} (A2/C2). These are usually attributed to the following two redox reactions:[34]

$$Co_3O_4 + OH^- + H_2O \longleftrightarrow 3CoOOH + e^- \; (1.22\ V_{RHE}) \quad (1)$$

$$CoOOH + OH^- \longleftrightarrow CoO_2 + H_2O + e^- \; (1.56\ V_{RHE}) \quad (2)$$

However, the formation of CoO_2 at 1.56 V is not undisputed. Studies of $Co(OH)_2$ in the OER range suggested transformation into CoOOH at 1.58 V.[35] Our very recent SXRD/XAS studies of these Co oxide films in pH 13 electrolyte showed that the Co oxidation state in the skin layer is 3+ up to 1.65 V, suggesting the absence of a measurable amount of Co^{4+}.[18]

Oxygen evolution commences at potentials ≥ 1.60 V. Figures 3j compares for Co_3O_4 and CoOOH the OER Tafel plots measured at different pH. The Tafel slope *b* gradually changes from close to ~50 mV/decade at pH 13 up to ~80 mV/decade at pH 7, 8 and 10 (see Table 1), which suggests a change of the OER rate determining step on both catalysts.[36,37] This change in Tafel slope with pH is reversible, because a very similar *b* value is found for all measurements at pH 13. However, there is a progressive deactivation of the Co_3O_4 catalyst at pH 13 along the sequence of measurements, indicated by a current density decrease and a downward shift of the Tafel plot.

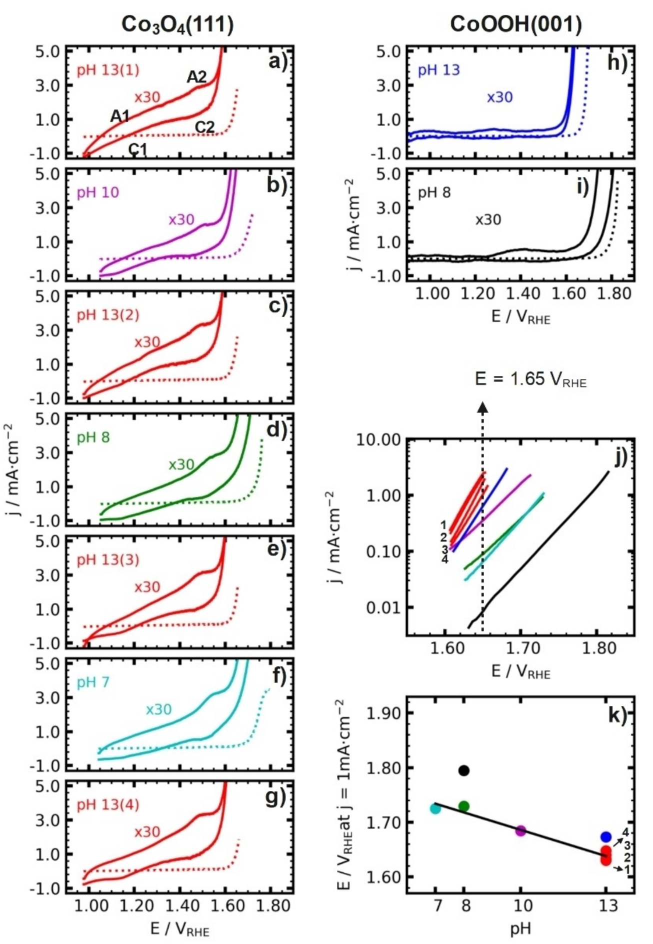

Figure 3. Cyclic voltammograms (dotted lines) of the (*a*-g) Co_3O_4 and (h, i) CoOOH catalyst in electrolytes of different pH (sweep rate 5 mV/s, for Co_3O_4 and 10 mV/s for CoOOH, iR-corrected). To show the CV in the pre-OER regime the current density was multiplied by a factor 30 (solid lines). (j) Tafel plots in the OER region, extracted from the iR-corrected potential scan in positive direction of the CVs. For pHs 7 and 8, the pseudo-capacitive current was subtracted. For the 4 measurements at pH 13 the number of the measurement in the sequence is given. (k) pH dependence of the OER overpotential at a constant current density of 1 mA/cm².

The Tafel plots and Figure 3k show that the overpotential necessary to reach a current density of 1 mA/cm² is generally increasing with decreasing pH for Co_3O_4 and CoOOH. This supports that the OER mechanism or its rate-limiting step is changing with pH, because the data are plotted versus RHE. However, no substantial difference between pH 7 and pH 8 phosphate buffer is found for Co_3O_4. This behavior resembles that of the CoCat catalyst formed in phosphate solution, for which likewise no potential dependence is found on the RHE scale at neutral pH.[38] At pH 13, the Tafel plot of CoOOH is only ≈ 25 mV shifted positively with respect to Co_3O_4, which may be

Table 1. Structural and electrochemical properties of Co_3O_4 in electrolytes of different pH. Shown are the OER Tafel slopes (*b*), current densities at 1.65 V ($j_{1.65\,V}$) obtained from the CVs, the grain size ($d_\perp/d_{||}$), and the absolute values of the associated changes in vertical and horizontal grain size ($\Delta d_\perp$, $\Delta d_{||}$) and strain ($\Delta\varepsilon_\perp$, $\Delta\varepsilon_{||}$) between 1.05 and 1.60 V. The values were taken from a floating average of the measurements with ±10 data points (solid lines in Figure 5) and correspond to the mean value of the positive and negative potential sweep. The errors (given in parenthesis) correspond to the standard deviations estimated from the fluctuations around the mean value over the entire CV of the average curves. The data are given in the order of the measurement.

pH	*b* (mV/decade)	$j_{1.65\,V}$ ($mAcm^{-2}$)	$d_{\parallel}$ (nm)	$\Delta d_{\parallel}$ (nm)	$d_\perp$ (nm)	$\Delta d_\perp$ (nm)	$\Delta\varepsilon_{\parallel}$ (%)	$\Delta\varepsilon_\perp$ (%)
13(1)	50	2.384	19.02(1)	0.19(2)	15.09(1)	0.40(2)	0.005(1)	0.120(1)
10	74	0.372	18.80(1)	0.20(2)	14.72(1)	0.41(2)	0.015(1)	0.125(1)
10	73	0.376	18.82(1)	0.19(2)	14.67(1)	0.37(1)	0.015(1)	0.125(1)
10	79	0.353	18.82(1)	0.20(2)	14.67(1)	0.42(1)	0.022(1)	0.125(1)
13(2)	49	2.140	18.90(1)	0.23(2)	14.81(1)	0.40(1)	0.015(1)	0.120(1)
8	75	0.115	18.89(1)	0.18(2)	14.66(1)	0.41(1)	0.026(1)	0.170(1)
8	76	0.106	18.86(1)	0.16(2)	14.60(1)	0.38(1)	0.022(1)	0.170(1)
8	86	0.088	18.85(1)	0.15(2)	14.54(1)	0.37(2)	0.025(1)	0.170(1)
13(3)	47	1.677	18.91(1)	0.27(2)	14.70(1)	0.36(1)	0.034(1)	0.130(2)
7	77	0.065	18.79(1)	0.19(3)	14.60(1)	0.50(2)	0.040(1)	0.180(2)
13(4)	55	1.027	18.79(1)	0.27(2)	14.67(1)	0.48(2)	0.044(1)	0.130(2)

partly accounted for by the different ECSA of these samples. At pH 8, the shift increases to 60 mV, i.e., the spinel oxide seems to be a better catalyst than CoOOH in neutral electrolyte.

2.3. Operando Surface X-Ray Diffraction Studies

The potential-dependent changes in the structure of the oxide film for solutions of different pH were determined by *operando* SXRD measurements, using the methodology employed in our previous work.[16,17] In these studies, X-ray surface diffraction images of Co oxide Bragg peaks were continuously collected during cyclic voltammograms. To determine the structural changes along a CV, these Bragg peak images were analyzed as described in section 2.2. Below, we discuss the potential dependent changes in the vertical (i.e., surface-normal) and horizontal (i.e., in-plane) lattice strain ($\Delta\varepsilon_\perp$ and $\Delta\varepsilon_{||}$) and grain size ($\Delta d_\perp$ and $\Delta d_{||}$) of the oxide films, taking as reference the state of the oxide structure that was measured at 1.05 V. The pH was varied by employing a series of electrolyte exchanges at open circuit potential (see section 2.2).

We first discuss the case of the CoOOH(001) film, which was investigated by monitoring the (017) Bragg peak (Figure 4). The data demonstrate that the oxyhydroxide film is structurally stable at pH 13 (left column) as well as at neutral pH 8 (right column). Both the strains $\Delta\varepsilon_{\perp,||}$ and crystallite size $\Delta d_{\perp,||}$ stay independent of the applied potential within the accuracy of the determination. The result at pH 13 is in accordance with our previous studies at this pH.[16] The novelty here is the stability of the CoOOH(001) film in neutral electrolyte over a wide range of potentials, including the OER region.

In contrast, Co_3O_4 exhibits noticeable potential-dependent structural changes. Figure 5 shows selected data of an *operando* SXRD experiment performed in electrolytes of different pH with the same sample (see Figure S1 for complete data set). The use of the same sample is crucial to avoid complications arising from the influence of the film morphology on the structural response.[17] The potential in the CVs was deliberately kept above 1.0 V to avoid Co_3O_4 conversion into $Co(OH)_2$, as found below 1 V in previous studies at pH 13[16] as well as in independent experiments at lower pH within this study. The data obtained at the different pH values is being displayed in Figure 5 in the order of their measurement (from left to right). The SXRD data were obtained by monitoring the $Co_3O_4(1\bar{1}3)$ Bragg peak and recorded simultaneously with the reflectivity signal and the electrochemical data shown in Figure 3a–g. They thus allow direct correlation of the potential-dependent structural changes with the OER activity. At all pH values the crystallite size ($d_{\perp,||}$) decreases towards more positive potentials, indicating the transformation of the outer part of the spinel lattice into the skin layer phase. Table 1 summarizes the overall changes in the structural parameters $\Delta\varepsilon_\perp$, $\Delta\varepsilon_{||}$, $\Delta d_\perp$, and $\Delta d_{||}$ between the lower potential limit of 1.05 V and 1.60 V (indicated by dashed vertical lines in Figure 5), i.e., a potential near the onset of the OER. Here, the average of values obtained in the positive and negative going potential scan was taken to reduce the effect of hysteresis (marked by crosses in Figure 5). In addition, the absolute grain sizes and the corresponding OER Tafel slopes and currents at 1.65 V are given for all data sets in table 1.

Overall, the structural changes are reversible at all pH values, reproducible in subsequent potential sweeps, and occur predominantly in the pre-OER regime. Complementary potential step experiments (Supporting Information, Section S1 and Figure S2) indicate that the process is fast. More than 80% of the changes in strain and skin layer thickness occur within the first second after the potential step, followed by a slower relaxation on the order of one minute in which a steady state structure is reached. This demonstrates that the structural changes in Figure 5 are a genuine potential effect and that the hysteresis stems from kinetics.

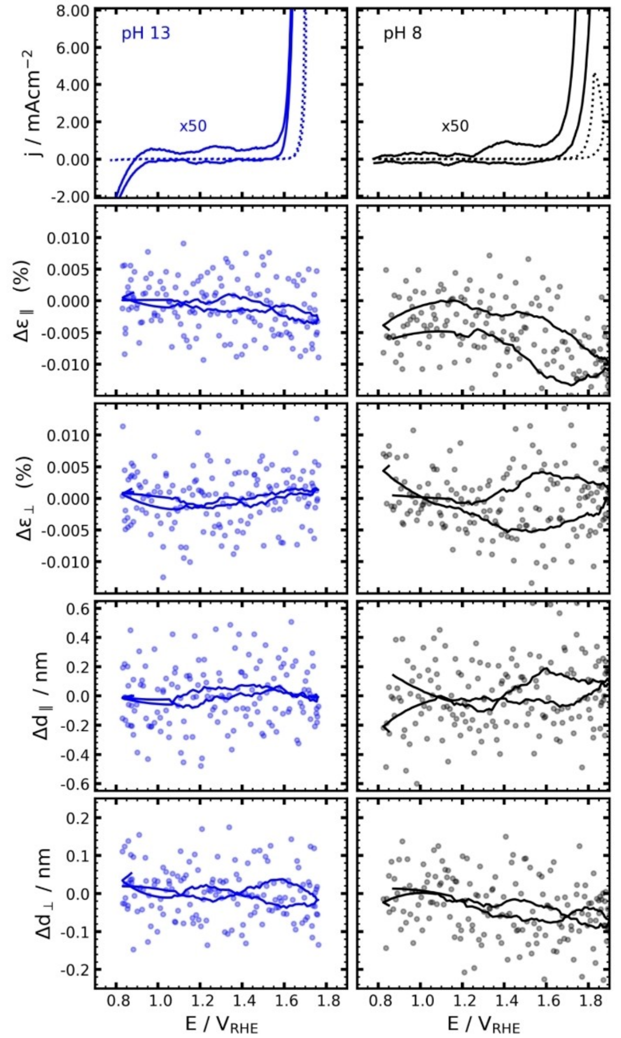

Figure 4. *Operando* SXRD results, showing the structural changes in a CoOOH(001) film on Au(111) during three potential cycles at pH 13 and pH 8 (scan rate 10 mV/s). Each column displays (from top to bottom) the electrochemical current density *j* and the variations of the horizontal strain $\Delta\varepsilon_{\parallel}$, the vertical strain $\Delta\varepsilon_{\perp}$, the horizontal crystallite grain size $\Delta d_{\parallel}$, and the vertical crystallite grain size $\Delta d_{\perp}$. The data were obtained from the variation of the CoOOH(017) Bragg reflection during the CVs shown in the upper panel and are given versus the iR-corrected potential. Before and after the potential cycles, the potential was kept at 1.4 V (pH 13) and 1.15 V (pH 8), respectively.

The following general trends are observed at all pH: (i) The unit cell volume of the spinel reversibly shrinks with potential because $\Delta\varepsilon_{\perp}$ and $\Delta\varepsilon_{||}$ are both <0; (ii) The crystallite size reversibly decreases by a fraction of a nanometer in both directions ($|\Delta d_{\perp}|$ and $|\Delta d_{||}| < 1$ nm); (iii) The strain changes and the change in crystallite size are rather anisotropic, since the absolute value of $\Delta\varepsilon_{\perp}$ is larger than $\Delta\varepsilon_{||}$ by a factor 4–5 and $\Delta d_{\perp} \approx 2\Delta d_{||}$. All these structural changes occur over a wide potential range that starts significantly below the onset of the OER. These trends are in qualitative agreement with our previous studies of Co_3O_4 in 0.1 M NaOH,[16,17] where we concluded that the reversible changes in average grain size reflect the formation of a sub-nanometer thick defective $CoO_x(OH)_y$ layer on top of the Co_3O_4 film and that the presence of this skin layer induces the contraction of the Co_3O_4 unit cell within the bulk oxide. Furthermore, the anisotropy of the strain and grain size changes may also be explained by the epitaxial nature and morphology of the Co_3O_4 film.[17] Specifically, the employed Co_3O_4 film features a morphology with large triangular islands with a flat (111)-oriented top, consisting of several closed packed grains separated by grain boundaries (see inset of Figure 2). As shown in Ref.,[17] in the case of the present morphology, the skin layer can only form on the outer facets of the islands that are exposed to the electrolyte but not inside the grain boundaries, resulting in significantly lower values of the in-plane structural parameters (the measurements by SXRD represent an average of all grains, i.e., grains with outer side walls as well as inner grains). For this reason, $\Delta d_{||}$ is not twice the value of $\Delta d_{\perp}$, as would be expected for a uniform skin layer thickness of freestanding islands, but much smaller. In addition, the in-plane strain $\Delta\varepsilon_{||}$ is also reduced by epitaxial clamping to the Au substrate.

We next discuss the influence of the pH on these structural parameters. In the sequence of experiments in Figure 5, the $\Delta d_{\perp}$ and $\Delta d_{||}$ values as well as the strain changes $\Delta\varepsilon_{\perp}$ and $\Delta\varepsilon_{||}$ appear slightly larger with decreasing pH, indicating the formation of thicker skin layers. However, this effect is largely related to the higher upper potential limit employed at lower pH values, because the skin layer continues to thicken with increasing potential in the OER range.[16] The results given in Table 1 and Figure 6a, where the structural changes over the same potential range are compared, show that this effect on $\Delta d_{\perp}$ and $\Delta d_{||}$ is negligible. Only at the end of the measurements ($pH > 8$) a small increase in $\Delta d_{\perp}$ and $\Delta d_{||}$ is observed. This increase is mostly caused by slow irreversible structural changes of the oxide film structure (see Figure 6a), which manifest as a continuous increase in $\Delta\varepsilon$ and Δd.

Close inspection of the structural data, especially those obtained during the potential sweep in positive direction, indicate the presence of two potential regions with different behaviors. This is most clearly seen in the data for $\Delta\varepsilon_{||}$. Here, we observe at more negative potentials either no (pH 10 and pH 13/1, 2) or only weak (pH 8, pH 7, and pH 13/3, 4) changes with potential; at more positive potentials the rate of change in $\Delta\varepsilon_{||}$ with potential is substantially larger. The crossover occurs at a clearly defined transition potential, namely the potential of peak A2 in the CV. This suggests that at this potential the skin layer formation becomes more efficient. A nearly linear change of $\Delta\varepsilon_{||}$ with potential is observed both negative (region I) and positive (region II) of this transition potential (marked exemplarily in the data set for pH 10). A similar effect is also seen in the $\Delta\varepsilon_{\perp}$ data. However, here the slope is already large in region I and increases only slightly in region II. Furthermore, these changes are also correlated well with changes in the rate of skin layer formation. Specifically, $\Delta d_{||}$ decrease in region I only weakly with increasing potential but with a much larger slope in region II. In vertical direction ($\Delta d_{\perp}$), the differences between region I and II are less pronounced, similar as in the case of the $\Delta\varepsilon_{\perp}$ data. Similar behavior was found also for other Co_3O_4 films, although the changes between regions I and II are differently

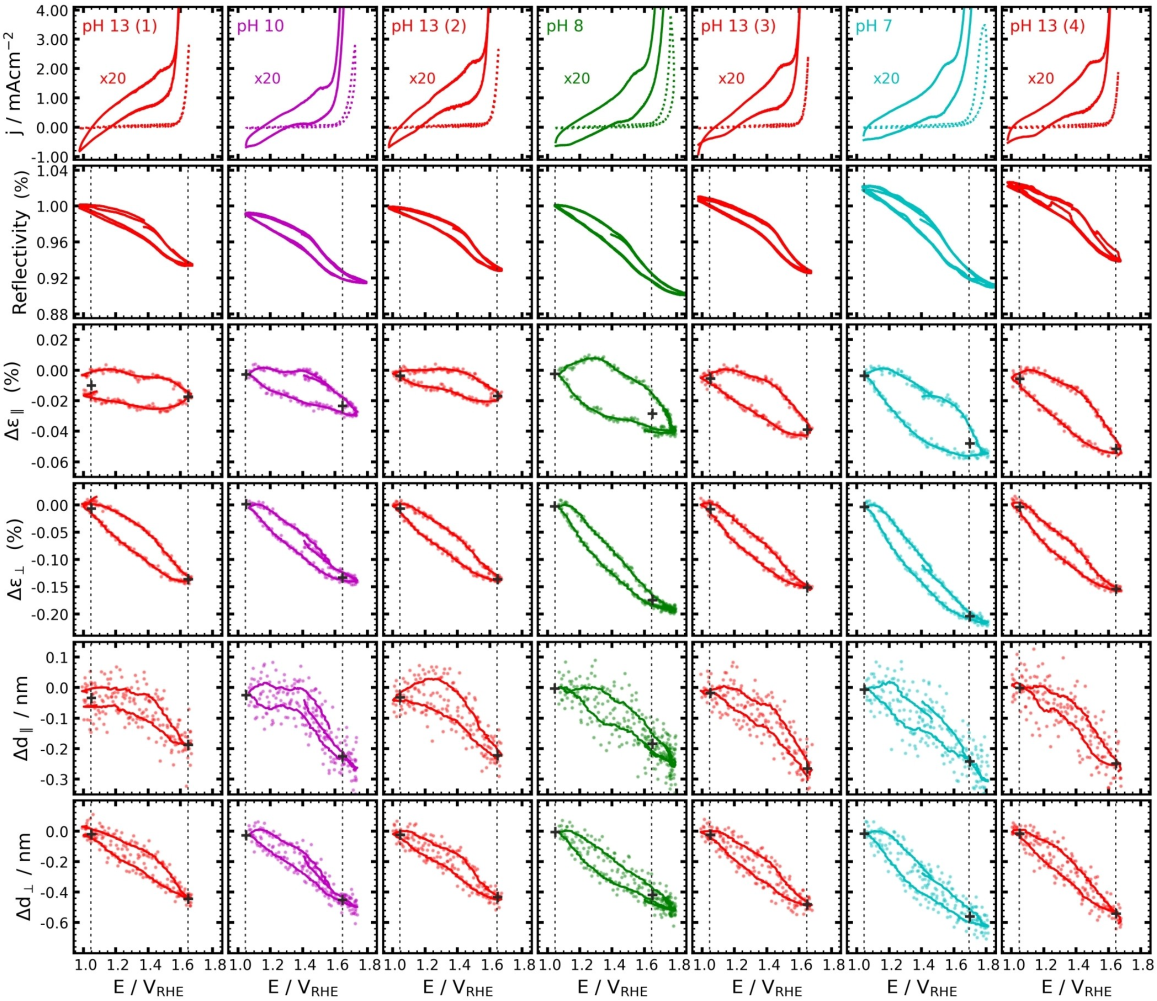

Figure 5. *Operando* SXRD results, showing the structural changes in a Co$_3$O$_4$(111) film on Au(111) in electrolytes of different pH during cyclic voltammograms (scan rate 5 mV/s). The data were recorded on the same Co$_3$O$_4$ sample and are selected from the full dataset (Figure S1). They are displayed in the figure (from left to right) following the measurement sequence. Each column shows (from top to bottom) the electrochemical current density *j*, with the double-layer region being scaled by a factor of 20 for better visibility (solid lines), the optical reflectivity, normalized to the initial value of the as prepared sample, and the variations of the horizontal strain $\Delta\varepsilon_{\parallel}$, the vertical strain $\Delta\varepsilon_{\perp}$, the horizontal crystallite grain size $\Delta d_{\parallel}$, and the vertical crystallite grain size $\Delta d_{\perp}$. The structural data were obtained from the variation of the Co$_3$O$_4$(1$\bar{1}$3) Bragg reflection during the CVs shown in the upper panel and are given versus the iR-corrected potential. Potentials and values used for the data given in Table 1 are marked by dashed lines and crosses, respectively.

pronounced, depending on the sample. These observations show that strain and skin layer thickness are directly correlated with each other and support our previous explanation that the strain in the spinel lattice is induced by the restructuring of the near-surface lattice into the skin layer.[17] It is noted that in neutral solution (pH 7 and 8) the difference between regions I and II is much less distinct for all structural parameters.

Apart from the relative changes in the structural parameters between 1.05 and 1.6 V, we also observe a gradual decrease of the absolute height $d_{\perp}$ and lateral size $d_{||}$ of the oxide grains at 1.05 V, by $\approx$0.4 and $\approx$0.2 nm, respectively, over the course of the experiment (see Table 1 and Figure 6b). These changes indicate dissolution of the oxide grains on the order of one Co atomic layer between the first and the last measurement at pH 13. In each step to lower pH values, a noticeable decrease is found, whereas the subsequent increase back to pH 13 results in partial reformation of the oxide. These effect will be discussed in more detail in section 4.2.

In addition, the simultaneously measured optical reflectivity *R* of the film reflects the changes in the oxide structure found by SXRD. The magnitude of the changes Δ*R* over the potential cycle increases together with the increasing magnitude of the structural changes over the experiment. Furthermore, also the transitions between regions I and II are clearly recognizable. As shown before,[16] the changes in *R* are proportional to the pseudo-capacitive charge transfer. The increase in Δ*R* between pH 13(1) and pH 13(4) therefore indicates the increasing charge required for forming the thicker skin layer. The total increase in the *R* value at 1.05 V over the pH sequence is most likely related to the decreasing oxide film thickness, because of increasing back-reflection by the Au substrate, which has a higher optical reflectance.

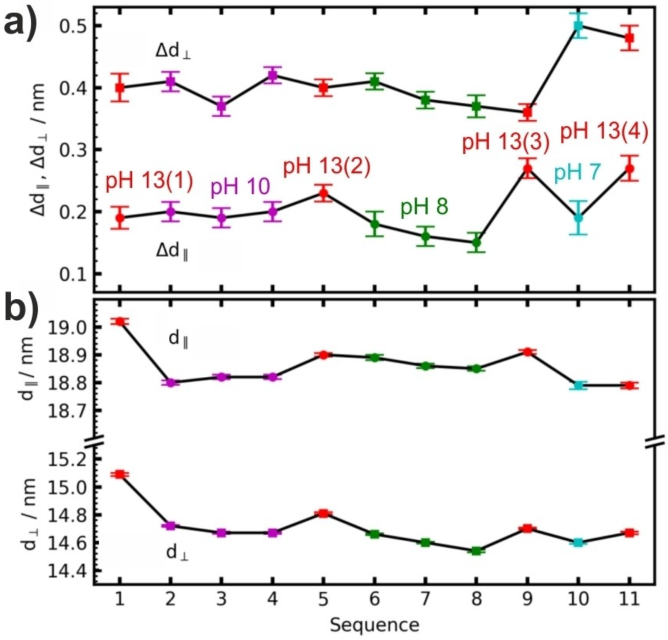

Figure 6. (a) Potential-dependent changes in horizontal and vertical grain size $\Delta d_{\parallel}$ and $\Delta d_{\perp}$ between 1.05 and 1.6 V and of (b) the absolute horizontal and vertical grain sizes $d_{\parallel}$ and $d_{\perp}$ at 1.05 V over the course of the experiment. At each point in the sequence 2–3 consecutive potential cycles of the type shown in Figure 5 were recorded. Results for the positive and negative scan were averaged to reduce the effect of the hysteresis.

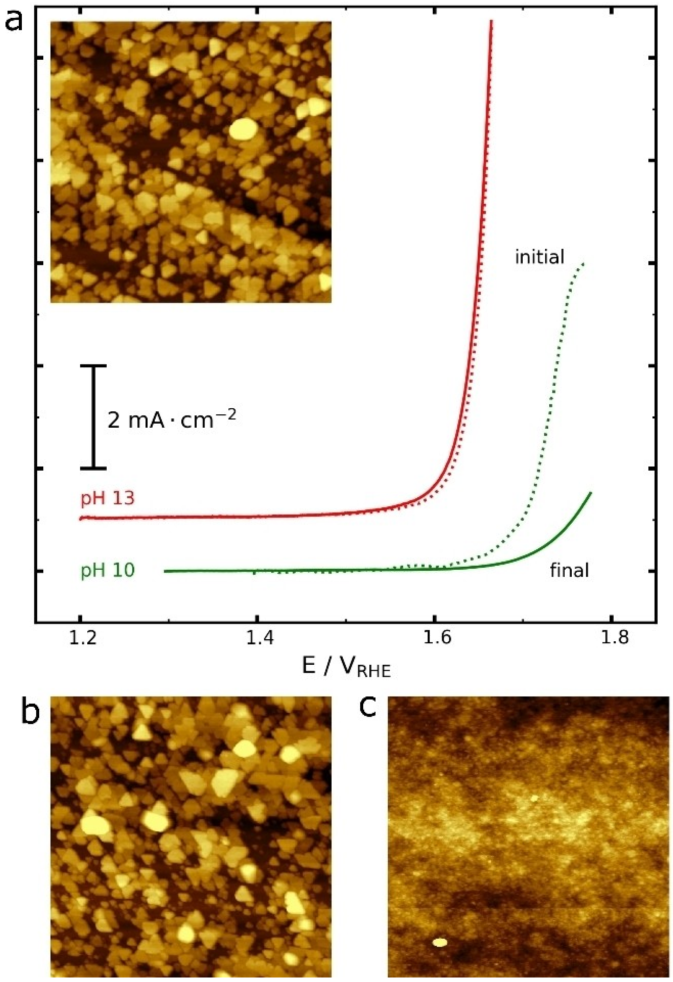

Figure 7. Effect of 2 hours of potential cycles and steps into the OER regime in pH 13 and pH 10 electrolyte. (a) CVs corresponding to the first (dashed line) and last (solid line) cycle of the experiments in pH 13 (red) and pH 10 (green). AFM images (1x1 μm^2) obtained before (a, inset) and after these electrochemical measurements in (b) pH 13 and (c) pH 10 electrolyte.

2.4. Ex Situ AFM and Electrochemical Studies of Irreversible Structural Changes

The *ex-situ* AFM image of the Co_3O_4 films after a sequence of experiment such as depicted in Figure 5, showed no obvious changes in the film morphology (Figure S3). This is consistent with the small but irreversible changes of the oxide grains detected by *operando* SXRD, which remain on the sub-nanometer length scale and thus are below the resolution of the AFM technique.

To investigate the stability of the film under more demanding conditions, we performed additional *ex situ* AFM and CV measurements. Figure 7a compares the initial CV and the one measured after 2 h of potential cycles at different scan rates and potential steps between 1 V and within the OER regime. At pH 13 (red lines), the CV remains unchanged and the topography of the sample (Figure 7b) is again essentially identical to that of the as prepared sample on the scale of the AFM observations. The sample therefore seems to be highly stable in 0.1 M NaOH even in harsh conditions.

In contrast, the sample seems unstable at pH 10. The current density strongly decreases after the same electrochemical treatment (Figure 7a, green lines), indicating that the sample deactivates. The Tafel slope changes from 80 to 100 mV/dec. This change may be related to changes in the local pH near the electrode surface, caused by insufficient mass transport in the SXRD cell and the limited buffering capability of the used electrolyte. The change in the CV is accompanied by a drastic modification of the film topography (Figure 7c). The characteristic triangular oxide islands found on the as-prepared sample, are no longer visible. The surface of the film appears featureless. A similar morphology was also observed after similar extensive treatment in pH 8 and 7 (Figure S4). Here, also some holes in the films were found that went down to the Au substrate, indicating complete dissolution of the oxide in these areas. Obviously the Co_3O_4 film is highly stable under strongly alkaline conditions, but prone to irreversible restructuring at pH 10 or lower, which may be partly related to changes in local pH.

3. Discussion

3.1. Overall Structural Behavior of CoOOH and Co3O4 in Neutral to Alkaline Solutions

The presented results confirm that the CoOOH and Co_3O_4 films are perfectly stable at pH 13 (Figure 6), in agreement with our past *operando* SXRD results (see introduction). The CoOOH films are also stable at neutral pH and their surface structure remains apparently unchanged over a wide potential range.

In the case of the spinel oxide, the surface is progressively covered by a skin layer with increasing potential in the pre-OER region and there is a contraction of the unit cell of the spinel oxide, which is induced by strongly mechanical coupling with the skin layer.[17] Stepping the potential back to values negative of about 1.15 V restores the original structure within a few seconds. In particular, the skin is recrystallized into Co_3O_4. Overall, this picture holds also at pH values below 13. However, our data indicate slow irreversible changes upon exposure of the sample to lower pH. Before discussing this pH-induced irreversible restructuring of the film and the influence of pH on the OER mechanism in the following sections, we here address observations that are common at all pH values and are associated with the skin layer nucleation and growth.

In all electrolytes the skin layer starts to form at potentials close to the Co_3O_4/CoOOH equilibrium potential of 1.22 V (Equation (1)). This provides strong evidence that the skin layer formation is driven by the oxide electrochemistry in aqueous solution. The potential dependent thickening of the skin layer is divided into two regions I and II (see Figure 5). In region I, starting at about 1.15 V, formation of a skin layer starts, as seen most clearly in the data for $\Delta d_\perp$. In region II, further thickening of $\Delta d_\perp$ and $\Delta d_{||}$ is found, but with an increased rate as compared to region I. In pH 13 and pH 10 solution, the change with potential in vertical direction, $d(\Delta d_\perp)/dE$, approximately doubles, whereas the corresponding in-plane change, $d(\Delta d_{||})/dE$, increases by at least a factor of 10. The transition between regions I and II starts near the onset potential of peak A2 in the corresponding CVs (see section 3.3). Consequently, peak A2 is indicating a change in the skin layer growth behavior rather than its nucleation. For a detailed microscopic interpretation of the origin of this transition in skin layer growth, further studies will be needed.

3.2. Influence of pH on the Skin Layer Formation on Co3O4

As already found in previous work,[16,17] the Co_3O_4 films are perfectly stable at pH 13. However, according to the results shown in Figure 6, slight Co_3O_4 dissolution occurs in electrolytes of pH ≤ 10, resulting in loss of sub-nanometer amounts of the oxide under the conditions of the experiment shown in Figure 5. Such dissolution may be expected on the basis of thermodynamic considerations,[39] especially under OER conditions where a decrease of the surface pH may be expected. Experimental evidence that such dissolution is also kinetically possible for well-ordered (111)-oriented films was found in recent studies for thin epitaxial Co_3O_4(111) films deposited by physical vapor deposition, both by ICP-MS measurements of the dissolved Co[19] as well as by STM observations of terrace roughening.[22] Further evidence of irreversible structural changes and dissolution of the oxide is found in our AFM observations after long-term potential cycling (see section 3.4).

Together with the film dissolution, we also observe a gradual increase in the potential-dependent changes of strain $\Delta\varepsilon_{\perp,||}$ and grain size $\Delta d_{\perp,||}$ (see Table 1) as well as the associated average skin layer thickness $\langle d_{skin}\rangle = \Delta V_{skin}/A$ (Figure 8a) where A is the geometric surface area and ΔV_{skin} the volume of crystalline Co_3O_4 that is reversibly converted into the skin layer (see supporting information section S2 for details). Following our previous results where we found the skin layer volume to increase with rougher Co_3O_4 surface morphology,[17] this increase in $\langle d_{skin}\rangle$ may be attributed to irreversible roughening of the oxide film by exposure to an electrolyte of pH lower than 8 (indicated schematically in Figure 9).

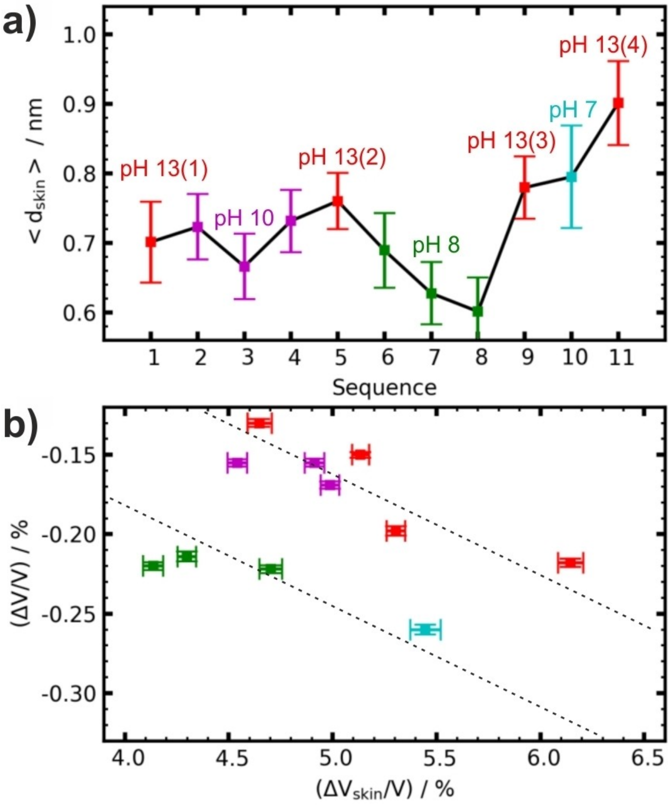

Figure 8. Effect of pH and time on the structural changes between 1.05 to 1.6 V_{RHE}. (a) Evolution of average skin layer thickness $<d_{skin}>$ over the course of the experiment. (b) Relative change of the unit cell volume in the spinel lattice of the Co_3O_4 grains as function of the fraction of the oxide that is converted into the skin layer. Dashed lines indicate the linear relationship found in Ref.[17] at pH 13.

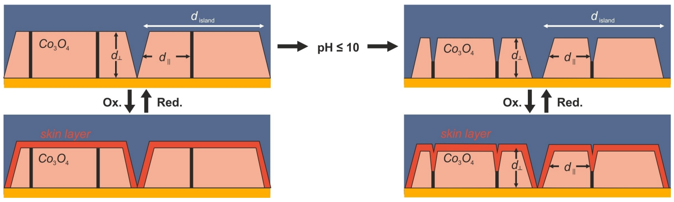

Figure 9. Schematic illustration of the evolution of the Co_3O_4 film morphology upon potential cycles at pH 13 (a) and pH ≤ 10 (b). At pH 13 the morphology stays stable. At lower pH irreversible Co dissolution promotes surface roughening and concomitant increases in skin layer volume.

Further insight into the role of pH in the surface structural transformation of Co_3O_4 can be obtained by correlating the skin volume fraction (V_{skin}/V) with the changes in relative unit cell volume ($\Delta V/V$) obtained from the strain changes $\Delta\varepsilon_{\perp,||}$ (supporting information section S2), as shown in Figure 8b. First, all data points measured at pH 13 are reasonably well described by a linear dependency (dotted lines). The linear change of $\Delta V/V$ with $\Delta V_{skin}/V$ is very similar to that found in our previous work on Co_3O_4 samples of increasingly rougher surface morphology (indicated by dashed lines) and can be explained by epitaxial strain in the spinel lattice that is induced by the skin layer.[17]

The second remarkable observation in Figure 8b concerns the position of data points measured at other pH values. While those at pH 10 roughly follow the linear dependency found at pH 13, those measured at pH 8 and 7 are clearly off. Specifically, the values of $\Delta V/V$ are offset to more negative values than those in 0.1 M NaOH at the same $\Delta V_{skin}/V$. Considering that the $\Delta V/V$ values return to the original linear relationship after exchanging the pH back from the neutral regime to pH 13, we assign the deviating behavior in the neutral electrolytes to variations of the strain within the skin layer and the coupling of this strain into the spinel lattice. According to Figure 8, this difference is not correlated to differences in the average skin thickness $\langle d_{skin} \rangle$ in the neutral electrolytes and therefore has to be related to a different structure or composition of the skin layer. We attribute this behavior to the incorporation of phosphates anions within the skin layer, as also detected by *ex situ* XPS measurements after OER in pH 7 phosphate buffer solution.[15] This might explain why the data points measured at pH 8 and 7 exhibit a linear dependency (dashed line) that is lower and roughly parallel to that found at pH 13. The phosphate that is present within the skin layer is apparently largely expelled from the surface region upon recrystallization of the skin into Co_3O_4 (at 1 V_{RHE}) because the sample reverts to the original $\Delta V/V$ - $\Delta V_{skin}/V$ dependency after changing the electrolyte back to 0.1 M NaOH.

Also other observations support the presence of an altered skin layer in the phosphate buffer solutions (pH 7 and 8). In the voltammograms, the peak A2 is located in between 1.40 and 1.45 V, which is similar to observations for the CoCat electrocatalyst.[40] The slight difference in peak potential at pH 7–8 as compared to pH 13 and 10 solution found in our study may thus result from the incorporation of phosphate in the skin layer, similar as during formation of the CoCat. Furthermore, the anisotropy between $\Delta d_{||}$ and $\Delta d_{\perp}$ is less pronounced at pH 7 and 8 and the potential dependencies in regions I and II do not differ significantly. This suggests again that the skin layer formation in presence and absence of phosphate differs noticeably.

3.3. Influence of pH on Electrocatalytic Properties

We estimated the OER turnover frequency (TOF) at 1.65 V at different pHs for Co_3O_4 and CoOOH. The TOF is defined as $TOF = \frac{j_{OER}}{z e_0 n_{Co}}$, where n_{Co} is the total number of Co atoms per geometrical surface area of the electrode that are able to promote the OER, $z = 4$, $e_0 = 1.6 \cdot 10^{-19}\ C$ is the elementary charge, and j_{OER} is the OER current density. In the case of CoOOH, the film is atomically flat and the surface structure remains unaltered in pre-OER and in OER regime (Figure 4).[16,33] Therefore, $n_{Co} = 1.42 \cdot 10^{15}\ cm^{-2}$ corresponding to the hexagonal unit cell of the surface ($a = 0.2851\ nm$).[17,33] For Co_3O_4 films in pH 13 electrolyte, the skin layer was previously shown to be a three-dimensional reaction zone for the OER.[17] Therefore, $n_{Co} = 4.54 \cdot 10^{15}\ cm^{-2} \cdot \langle d_{skin} \rangle$, where $\langle d_{skin} \rangle$ is in nm because the volume density of Co ions in Co_3O_4 is $4.54 \cdot 10^{22}$ cm^{-3}.

Figure 10a shows the pH-dependence of the TOF measured with CoOOH and Co_3O_4 films at 1.65 V. The intrinsic OER activity of CoOOH(001) (stars) is near that of Co_3O_4 (squares) at pH 13, in agreement with our previous work.[16] The first general trend is a decay of the TOF with decreasing pH for both oxides. The values at pH 8 are smaller by a factor 26–30 than at pH 13 for Co_3O_4. Comparable deactivation is found for CoOOH although the error of the TOF at pH 8 is large, because the OER current at 1.65 V is much smaller than the pseudo-capacitive current.

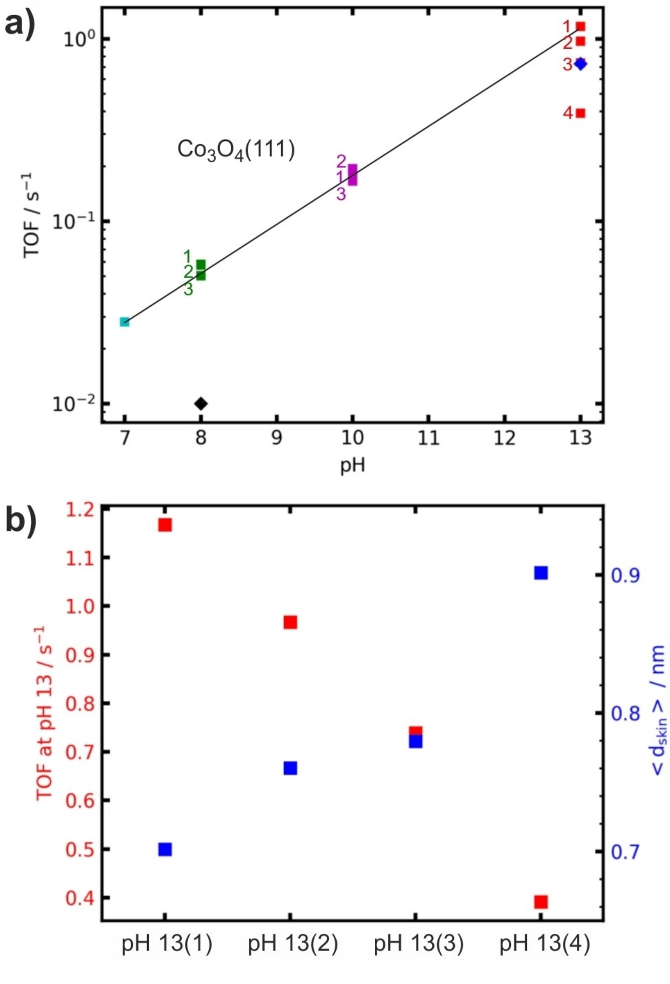

Figure 10. (a) pH dependence of the TOF values at 1.65 V_{RHE} (right y axis). The same color scheme as in Figure 3 is used. Numbers indicate the number of the measurements at the corresponding pH. (b) Changes in the TOF and $\langle d_{skin} \rangle$ values, measured at pH 13 during the measurement sequence.

More specifically, for Co_3O_4, the $log(TOF)$ is nearly a linear function of the pH with a slope $d\ log(TOF)/d\ pH$ close to 0.2. This means that the TOF of Co_3O_4(111) films increases proportionally to $[OH^-]^{0.2}$. The sparser data set obtained on the CoOOH films indicates a similar reaction order. This OER deactivation at lower pH is accompanied with a change of the reaction mechanism, as indicated by the increase in Tafel slope at pH $\leq$ 10 for Co_3O_4 (Figure 3j and Table 1). The reaction order of 0.2 with respect to $[OH^-]$ is consistent with the survey by Giordano et al. for the reaction order of OER catalyst materials of 3d transition metals with oxidation state 3+ and spinel structure.[24] In that work, the non-zero reaction order was explained by sequential proton and electron transfer.

The second main information, displayed in Figure 10b, concerns the OER activity measured at pH 13, which progressively decays after each exposure of the sample to solution of lower pH. However, the OER mechanism stays unaltered at pH 13 because the Tafel slope returns to its initial value of ~50 mV/dec. (Figure 3j, Table 1). We emphasize that no deactivation of the catalyst takes place as long as it is kept in 0.1 M NaOH. In this case, the OER activity stays perfectly stable even after multiple cycling and harsh steady OER conditions and the film morphology remains very similar to the initial one (see section 3.4, Figure 7).

To explain the above catalyst deactivation, we infer that the surface of Co_3O_4 is cumulatively modified by specifically adsorbing anion species (carbonate, phosphate) during sample exposure to solutions of pH $\leq$ 10. As already discussed in section 4.2, there is indirect evidence that phosphates get incorporated into the skin layer during its formation in the solutions of pH 7 and 8. One single potential cycle with skin layer formation/reduction in a solution of lower pH seems sufficient to irreversibly alter the catalyst activity measured at pH 13, because the relative decay of the TOF at pH 13 appears to be independent of the number of previous potential cycles conducted in the low-pH solution. Part of the phosphate must be staying in the near surface region upon exchanging the phosphate solution with 0.1 M NaOH. However, the data in Figure 8b suggest that the characteristic skin layer properties found in alkaline electrolyte, specifically the skin layer induced strain in the spinel, are immediately recovered upon changing the pH back to 13 (see section 4.2). These apparently contradictory observations may be reconciled, if the phosphate is not embedded in the skin layer, but chemisorbs on the interface between electrolyte and oxide (or on the oxide skin layer) and blocks access to the reactive zone underneath. Indeed, *ex situ* XPS studies of Co_3O_4(111) films found weak phosphate peaks after voltammetric studies in phosphate buffer.[19] Although those were assigned to residual bulk electrolyte, they may also result from adsorbed species. A similar poisoning by carbonates (pH 10) is also likely. The poisoning effect seems to be cumulative rather than specific to one type of anion (phosphates vs. carbonates) because the relative deactivation seems identical for all solutions of lower pH. To test this idea, it would be interesting to compare the data in Figure 10 with the intrinsic OER activity of CoCat, where phosphates are largely present. An accurate determination of n_{Co} for CoCat seems however challenging. More work is necessary to assess why and in which form phosphates and carbonates are remaining on the spinel oxide surface upon transfer to 0.1 M NaOH. The mechanism of Co active site poisoning by phosphates or carbonate needs also to be elucidated.

4. Conclusions

The results presented in this work demonstrate that the general surface structural behavior found for CoOOH and Co_3O_4 OER electrocatalysts at pH 13 persists down to the neutral pH range. Specifically, down to pH 7, CoOOH exhibits high structural stability whereas the near-surface region of Co_3O_4 is reversibly transformed in the pre-OER region. The thickness of the skin layer, in which the Co_3O_4 spinel lattice is transformed, is in the sub-nanometer range at all pH values. However, we also observe several noticeable differences of the Co_3O_4 structure and reactivity with decreasing pH:

- The specific properties of the skin layer seem to depend on the nature of the electrolyte. In particular, indirect indication for the incorporation of phosphate ions into the skin layer is found.
- The OER turnover frequency increases substantially with pH. The corresponding reaction order of the OER current at fixed potential vs. RHE is indicative of a reaction mechanism in which proton and energy transfer is partially decoupled.
- At pH $\leq$ 10, the oxide starts to dissolve and its average skin layer thickness increases, indicating roughening of the oxide.
- Exposure to solutions of pH $\leq$ 10 also leads to an irreversible decrease of the OER turnover frequency at pH 13, indicating catalyst deactivation.

In addition, the skin layer formation is found to be a two-stage process, in which the potential-dependent thickness change increases above the potential of the anodic peak A2 in the cyclic voltammogram.

In total, these results show that the reversible formation of a skin layer on Co_3O_4 is a phenomenon occurring in a wide range of electrolytes and that the local (near-surface) structure and OER activity of Co_3O_4 depends pronouncedly on the solution pH and composition. These effect thus have to be seriously considered in experimental as well as *ab initio* theory studies of the OER mechanism on these materials. While both CoOOH and Co_3O_4 epitaxial films have good OER activity, a well-defined surface orientation, and a high structural stability across a wide pH range, the potential-dependent structural transformation of the Co_3O_4 surface makes a mechanistic understanding of the OER reaction more difficult. In contrast, CoOOH(001) exhibit a stable surface structure that does not depend on potential or pH. Furthermore, the skin layer formed on top of Co_3O_4 is assumed to be similar in nature to CoOOH. Thus, the CoOOH samples may provide a good system to investigate the OER reaction mechanism and the true intrinsic effect of pH on the OER by *ab initio* modelling.

Acknowledgements

We gratefully acknowledge financial support for P.A., F.M., I.P. and M.B. by the Agence Nationale de la Recherche (ANR) and for C.Q., T.W., J.S., and O.M.M. by the Deutsche Forschungsgemeinschaft (DFG) via project EC-MEC (ANR-15-CE30–0024–01 and DFG 284207613) and for C.Q., C.H.S. and O.M.M. via the Collaborative Research Center SFB/TRR247 (project number 388390466) and the German Federal Ministry of Education and Research (BMBF) via project 05K19FK3. We acknowledge DESY (Hamburg, Germany), a member of the Helmholtz Association HGF, for the provision of experimental facilities. Parts of this research were carried out at PETRA III beamline P23 and we would like to thank D. Novikov and A. Khadiev for assistance in using the beamline during the experiment. Beamtime was allocated for proposals I-20180014 and I-20180835. Open Access funding enabled and organized by Projekt DEAL.

Conflict of Interests

There is no conflict of interest.

Data Availability Statement

The data that support the findings of this study are available from the corresponding author upon reasonable request.

Keywords: Electrochemistry · Heterogeneous catalysis · Water splitting · Interfaces · Transition metal oxides · X-ray diffraction · Operando studies

[1] I. Roger, M. A. Shipman, M. D. Symes, *Nat. Chem. Rev.* **2017**, *1*, 0003.
[2] N. S. Lewis, D. G. Nocera, *Proc. Nat. Acad. Sci.* **2006**, *103*, 15729–15735.
[3] M. W. Kanan, D. G. Nocera, *Science* **2008**, *321*, 1072–1075.
[4] R. L. Doyle, I. J. Godwin, M. P. Brandon, M. E. G. Lyons, *Phys. Chem. Chem. Phys.* **2013**, *15*, 13737–13783.
[5] C. C. L. McCrory, S. Jung, I. M. Ferrer, S. M. Chatman, J. C. Peters, T. F. Jaramillo, *J. Am. Chem. Soc.* **2015**, *137*, 4347–4357.
[6] M. S. Burke, L. J. Enman, A. S. Batchellor, S. Zou, S. W. Boettcher, *Chem. Mater.* **2015**, *27*, 7549–7558.
[7] N.-T. Suen, S.-F. Hung, Q. Quan, N. Zhang, Y.-J. Xu, H. M. Chen, *Chem. Soc. Rev.* **2017**, *46*, 337–365.
[8] M. S. Burke, M. G. Kast, L. Trotochaud, A. M. Smith, S. W. Boettcher, *J. Am. Chem. Soc.* **2015**, *137*, 3638–3648.
[9] C. Pirovano, G. Lodi, S. Trasatti, *J. Electrochem. Soc.* **1984**, *131*, C110–C110.
[10] Y. Surendranath, M. Dinca, D. G. Nocera, *J. Am. Chem. Soc.* **2009**, *131*, 2615–2620.
[11] A. J. Esswein, M. J. McMurdo, P. N. Ross, A. T. Bell, T. D. Tilley, *J. Phys. Chem. C* **2009**, *113*, 15068–15072.
[12] J. A. Koza, Z. He, A. S. Miller, J. A. Switzer, *Chem. Mater.* **2012**, *24*, 3567–3573.
[13] D. Friebel, M. Bajdich, B. S. Yeo, M. W. Louie, D. J. Miller, H. Sanchez Casalongue, F. Mbuga, T.-C. Weng, D. Nordlund, D. Sokaras, R. Alonso-Mori, A. T. Bell, A. Nilsson, *Phys. Chem. Chem. Phys.* **2013**, *15*, 17460–17467.
[14] A. Bergmann, E. Martinez-Moreno, D. Teschner, P. Chernev, M. Gliech, J. Ferreira de Araujo, T. Reier, H. Dau, P. Strasser, *Nat. Commun.* **2015**, *6*, 8625.
[15] A. Bergmann, T. E. Jones, E. Martinez Moreno, D. Teschner, P. Chernev, M. Gliech, T. Reier, H. Dau, P. Strasser, *Nat. Catal.* **2018**, *1*, 711–719.
[16] F. Reikowski, F. Maroun, I. Pacheco, T. Wiegmann, P. Allongue, J. Stettner, O. M. Magnussen, *ACS Catal.* **2019**, *9*, 3811–3821.
[17] T. Wiegmann, I. Pacheco, F. Reikowski, J. Stettner, C. R. Qiu, M. Bouvier, M. Bertram, F. Faisal, O. Brummel, J. Libuda, J. Drnec, P. Allongue, F. Maroun, O. M. Magnussen, *ACS Catal.* **2022**, *12*, 3256–3268.
[18] M. Bouvier, I. P. Bubi, T. Wiegmann, C. R. Qiu, P. Allongue, O. M. Magnussen, F. Maroun, *ACS Appl. Energ. Mater.* **2023**, *6*, 7335–7345.
[19] F. Faisal, M. Bertram, C. Stumm, S. Cherevko, S. Geiger, O. Kasian, Y. Lykhach, O. Lytken, K. J. J. Mayrhofer, O. Brummel, J. Libuda, *J. Phys. Chem. C* **2018**, *122*, 7236–7248.
[20] F. Faisal, C. Stumm, M. Bertram, F. Waidhas, Y. Lykhach, S. Cherevko, F. Xiang, M. Ammon, M. Vorokhta, B. Šmíd, T. Skála, N. Tsud, A. Neitzel, K. Beranová, K. C. Prince, S. Geiger, O. Kasian, T. Wähler, R. Schuster, M. A. Schneider, V. Matolín, K. J. J. Mayrhofer, O. Brummel, J. Libuda, *Nat. Mater.* **2018**, *17*, 592–598.
[21] E. M. Davis, A. Bergmann, C. Zhan, H. Kuhlenbeck, B. R. Cuenya, *Nat. Comm.* **2023**, *14*, 4791.
[22] E. M. Davis, A. Bergmann, H. Kuhlenbeck, B. R. Cuenya, *J. Am. Chem. Soc.* **2024**, *146*, 13770–13782.
[23] M. T. M. Koper, *Chem. Sci.* **2013**, *4*, 2710–2723.
[24] L. Giordano, B. H. Han, M. Risch, W. T. Hong, R. R. Rao, K. A. Stoerzinger, Y. Shao-Horn, *Catal. Today* **2016**, *262*, 2–10.
[25] J. B. Gerken, J. G. McAlpin, J. Y. C. Chen, M. L. Rigsby, W. H. Casey, R. D. Britt, S. S. Stahl, *J. Am. Chem. Soc.* **2011**, *133*, 14431–14442.
[26] J. S. Mondschein, J. F. Callejas, C. G. Read, J. Y. C. Chen, C. F. Holder, C. K. Badding, R. E. Schaak, *Chem. Mater.* **2017**, *29*, 950–957.
[27] M. Etzi Coller Pascuzzi, M. van Velzen, J. P. Hofmann, E. J. M. Hensen, *ChemCatChem* **2021**, *13*, 459–467.
[28] A. L. Li, S. Kong, C. X. Guo, H. Ooka, K. Adachi, D. Hashizume, Q. K. Jiang, H. X. Han, J. P. Xiao, R. Nakamura, *Nat. Catal.* **2022**, *5*, 109–118.
[29] J. Yu, F. A. Garces-Pineda, J. Gonzalez-Cobos, M. Pena-Diaz, C. Rogero, S. Gimenez, M. C. Spadaro, J. Arbiol, S. Barja, J. R. Galan-Mascaros, *Nat. Commun.* **2022**, *13*, 4341.
[30] S. Cherevko, *Curr. Opin. Electrochem.* **2023**, *38*, 101213.
[31] Z. Sheng, S. Wang, Q. Jiang, Y. Ni, C. Zhang, A. Ahmad, F. Song, *Catal. Sci. Technol.* **2023**, *13*, 4542–4549.
[32] C. Wang, R. Deng, M. Guo, Q. Zhang, *Int. J. Hydrogen Energy* **2023**, *48*, 31920–31942.
[33] I. Pacheco, M. Bouvier, O. M. Magnussen, P. Allongue, F. Maroun, *J. Electrochem. Soc.* **2023**, *170*, 012501.
[34] W. K. Behl, J. E. Toni, *J. Electroanal. Chem.* **1971**, *31*, 63–75.
[35] J. T. Mefford, A. R. Akbashev, M. K. Kang, C. L. Bentley, W. E. Gent, H. T. D. Deng, D. H. Alsem, Y. S. Yu, N. J. Salmon, D. A. Shapiro, P. R. Unwin, W. C. Chueh, *Nature* **2021**, *593*, 67–73.
[36] A. Damjanovic, A. Dey, J. O. M. Bockris, *Electrochim. Acta* **1966**, *11*, 791–814.
[37] J. O. M. Bockris, T. Otagawa, *J. Electrochem. Soc.* **1984**, *131*, 290–302.
[38] Y. Surendranath, M. W. Kanan, D. G. Nocera, *J. Am. Chem. Soc.* **2010**, *132*, 16501–16509.
[39] M. Bajdich, M. Garcia-Mota, A. Vojvodic, J. K. Noerskov, A. T. Bell, *J. Am. Chem. Soc.* **2013**, *135*, 13521–13530.
[40] M. Risch, F. Ringleb, M. Kohlhoff, P. Bogdanoff, P. Chernev, I. Zaharieva, H. Dau, *Energy Environ. Sci.* **2015**, *8*, 661–674.

Manuscript received: June 11, 2024
Revised manuscript received: August 22, 2024
Accepted manuscript online: August 28, 2024
Version of record online: October 26, 2024